CORA Cork Open Research Archive
Cartlann Taighde Oscailte Chorcaí

Title	High-bandwidth generation of duobinary and alternate-mark-inversion modulation formats using SOA-based signal processing
Authors	Dailey, James M.;Power, Mark J.;Webb, Rod P.;Manning, Robert J.
Publication date	2011-12-19
Original Citation	Dailey, J.M.; Power, M.J.; Webb, R.P.; Manning, R.J.; (2011) 'High-Bandwidth Generation of Duobinary and Alternate-Mark-Inversion Modulation Formats Using SOA-Based Signal Processing'. Optics Express, 19 (27):25954-25968.
Type of publication	Article (peer-reviewed)
Link to publisher's version	http://www.opticsinfobase.org/oe/abstract.cfm?URI=oe-19-27-25954 - 10.1364/OE.19.025954
Rights	© 2011, Optical Society of America. Open Access. - https://creativecommons.org/licenses/by/4.0/
Download date	2026-11-01 17:06:21
Item downloaded from	https://hdl.handle.net/10468/479

UCC
University College Cork, Ireland
Coláiste na hOllscoile Corcaigh



This paper appears in *Optics Express* and is made available as an electronic reprint with the permission of OSA. The paper can be found at the following URL on the OSA website:

http://www.opticsinfobase.org/oe/abstract.cfm?uri=oe-19-27-25954

Systematic or multiple reproduction or distribution to multiple locations via electronic or other means is prohibited and is subject to penalties under law.

High-bandwidth generation of duobinary and alternate-mark-inversion modulation formats using SOA-based signal processing

James M. Dailey, Mark J. Power, Roderick P. Webb, and Robert J. Manning
Tyndall National Institute & Department of Physics, University College Cork, Lee Maltings, Cork, Ireland
james.dailey@tyndall.ie

Abstract: We report on the novel all-optical generation of duobinary (DB) and alternate-mark-inversion (AMI) modulation formats at 42.6 Gb/s from an input on-off keyed signal. The modulation converter consists of two semiconductor optical amplifier (SOA)-based Mach-Zehnder interferometer gates. A detailed SOA model numerically confirms the operational principles and experimental data shows successful AMI and DB conversion at 42.6 Gb/s. We also predict that the operational bandwidth can be extended beyond 40 Gb/s by utilizing a new pattern-effect suppression scheme, and demonstrate dramatic reductions in patterning up to 160 Gb/s. We show an increasing trade-off between pattern-effect reduction and mean output power with increasing bitrate.

©2011 Optical Society of America

OCIS Codes: (060.0060) Fiber optics and optical communications; (070.4340) Nonlinear optical signal processing; (230.3750) Optical logic devices; (230.1150) All-optical devices; (250.4110) Modulators; (250.5980) Semiconductor optical amplifiers.

References and Links

1. P. J. Winzer and R. J. Essiambre, "Advanced Optical Modulation Formats," Proceedings of the IEEE **94**, 952-985 (2006).
2. J.D. Downie, A.B. Ruffin, and J. Hurley, "Ultra-low-loss optical fiber enabling purely passive 10 Gb/s PON systems with 100 km length," Optics Express **17**, 2392-2399 (2009), http://www.opticsinfobase.org/oe/abstract.cfm?URI=oe-17-4-2392.
3. A. H. Gnauck, X. Liu, X. Wei, D.M. Gill, and E.C. Burrows, "Comparison of modulation formats for 42.7-Gb/s single-channel transmission through 1980 km of SSMF," Photonics Technol. Lett. **16**, 909-911 (2004).
4. P. J. Winzer, A.H. Gnauck, G. Raybon, S. Chandrasekhar, Y. Su, and J. Leuthold, "40-Gb/s return-to-zero alternate-mark-inversion (RZ-AMI) transmission over 2000 km," Photonics Technol. Lett. **15**, 766-768 (2003).
5. K. S. Cheng and J. Conradi, "Reduction of pulse-to-pulse interaction using alternative RZ formats in 40-Gb/s systems," Photonics Technol. Lett. **14**, 98-100 (2002).
6. A. J. Price and N. Le Mercier, "Reduced bandwidth optical digital intensity modulation with improved chromatic dispersion tolerance," Electronics Letters **31**, 58-59 (1995).
7. R. S. Tucker, K. Hinton, and G. Raskutti, "Energy consumption limits in high-speed optical and electronic signal processing," Electronics Letters **43**, 906-908 (2007).
8. I. Kang, M.S. Rasras, L.L. Buhl, M. Dinu, G. Raybon, S. Cabot, M.A. Cappuzzo, L.L. Gomez, Y.Y. Chen, S.S. Patel, A.A. Piccirilli, J. Jaques, and C.C. Randy Giles, "High-Speed All-Optical Generation of Advanced Modulation Formats Using Photonic-Integrated All-Optical Format Converter," IEEE Journal of Selected Topics in Quantum Electronics, *Published Online*, http://ieeexplore.ieee.org/xpls/abs_all.jsp?arnumber=5771528.
9. J.M. Dailey, M.J. Power, R.P. Webb, and R.J. Manning, "All-Optical Modulation Converter for On-Off Keying to Duobinary and Alternate-Mark Inversion at 42.6 Gbps," in *CLEO/Europe 2011*, Munich, Germany, 2011, Paper CI4.1.
10. P. J. Winzer and J. Leuthold, "Return-to-zero modulator using a single NRZ drive signal and an optical delay interferometer," Photonics Technol. Lett. **13**, 1298-1300 (2001).
11. O. Leclerc, B. Lavigne, E. Balmefrezol, P. Brindel, L. Pierre, D. Rouvillain, and F. Seguineau, "Optical Regeneration at 40 Gb/s and Beyond," J. Lightwave Technol. **21**, 2779 (2003).
12. R. D. Gitlin, J. F. Hayes, and S. B. Weinstein, *Data Communication Principles* (Plenum Press, New York, 1992).

13. E. Jahn, N. Agrawal, M. Arbert, H.-J. Ehrke, D. Franke, R. Ludwig, W. Pieper, H.G. Weber, C.M. Weinert, "40 Gbit/s all-optical demultiplexing using a monolithically integrated Mach-Zehnder interferometer with semiconductor laser amplifiers," Electronics Letters **31**, 1857-1858 (1995).
14. J. M. Dailey, R. P. Webb, and R. J. Manning, "All-optical technique for modulation format conversion from on-off-keying to alternate-mark-inversion," Optics Express **18**, 21873-21882 (2010), http://www.opticsinfobase.org/oe/abstract.cfm?URI=oe-18-21-21873.
15. L. Billes, J.C. Simon, B. Kowalski, M. Henry, G. Michaud, P. Lamouler, and F. Alard, "20 Gbit/s optical 3R regenerator using SOA based Mach-Zehnder interferometer gate," in *11th International Conference on Integrated Optics and Optical Fibre Communications and 23rd European Conference on Optical Communications (IOCC-ECOC 1997)*, Edinburgh , UK, **2**, pg. 269-272.
16. J. M. Dailey and T. L. Koch, "Simple Rules for Optimizing Asymmetries in SOA-Based Mach-Zehnder Wavelength Converters," J. Lightwave Technol. **27**, 1480-1488 (2009).
17. R. P. Webb, J. M. Dailey, and R. J. Manning, "Pattern Compensation in SOA-based Gates," Optics Express **18**, 13502-13509 (2010), http://www.opticsinfobase.org/oe/abstract.cfm?URI=oe-18-13-13502.
18. T. Durhuus, B. Mikkelsen, C. Joergensen, S.L. Danielsen, and K.E. Stubkjaer, "All-optical wavelength conversion by semiconductor optical amplifiers," J. Lightwave Technol. **14**, 942-954 (1996).
19. G. Contestabile, A. Maruta, and K. Kitayama, "Gain Dynamics in Quantum-Dot Semiconductor Optical Amplifiers at 1550 nm," Photonics Technol. Lett. **22**, 987-989 (2010).
20. R.J. Manning, X. Yang, R.P. Webb, R. Giller, F.C. Garcia Gunning, and A.D. Ellis, "The turbo-switch - a novel technique to increase the high-speed response of SOAs for wavelength conversion," in *Optical Fiber Communication Conference*, Anaheim, CA, USA, 2006, Paper OWS8.
21. Y. Liu, E. Tangdiongga, Z. Li, S. Zhang, H. de Waardt, G.D. Khoe, and H.J.S. Dorren, "Error-free all-optical wavelength conversion at 160 gb/s using a semiconductor optical amplifier and an optical bandpass filter," J. Lightwave Technol. **24**, 230-236 (2006).
22. M. Nielsen and J. Mørk, "Bandwidth enhancement of SOA-based switches using optical filtering: theory and experimental verification," Optics Express **14**, 1260-1265 (2006), http://www.opticsexpress.org/abstract.cfm?URI=oe-14-3-1260.
23. S. Bischoff, M. L. Nielsen, and J. Mork, "Improving the all-optical response of SOAs using a modulated holding signal," J. Lightwave Technol. **22**, 1303-1308 (2004).
24. I. Kang, C. Dorrer, L. Zhang, M. Rasras, A. Bhardwaj, L. Buhl, S. Cabot, M. Dinu, M. Cappuzzo, L. Gomez, A. Wong-Foy, Y.F. Chen, D.T. Neilson, S. Patel, and J. Jaques, "Experimental investigation of pattern-dependent phase fluctuation in wavelength conversion and XOR operation using semiconductor optical amplifiers," in *31st European Conference on Optical Communication (ECOC 2005)*, Glasgow, UK, 2005, **2**, pg. 231-232.
25. M. L. Nielsen, J. Mørk, R. Suzuki, J. Sakaguchi, and Y. Ueno, "Experimental and theoretical investigation of the impact of ultra-fast carrier dynamics on high-speed SOA-based all-optical switches," Optics Express **14**, 331-347 (2006), http://www.opticsexpress.org/abstract.cfm?URI=oe-14-1-331.
26. R. J. Manning and D. A. O. Davies, "Three-wavelength device for all-optical signal processing," Opt. Lett. **19**, 889-991 (1994).
27. X. Jing, Z. Xinliang, and J. Mork, "Investigation of Patterning Effects in Ultrafast SOA-Based Optical Switches," IEEE Journal of Quantum Electronics **46**, 87-94 (2010).

---

1. Introduction

As engineers strive for novel ways to attain ultimate channel capacity over fiber and maximize the efficient use of network resources, attention has increasingly turned to the use of advanced modulation formats [1]. The pursuit of high-bandwidth transmission in long-haul core networks is dominated by research into phase-shift keying (PSK) and quadrature amplitude modulation (QAM) formats, which have increased spectral efficiency compared to non-return-to-zero (NRZ) and return-to-zero (RZ) on-off keying (OOK). Research also continues into other advanced modulation formats in network applications where fiber capacity is not the most important criterion. For example, Downie, *et al*, have recently exploited the duobinary modulation format over ultra-low-loss fiber in a long-reach PON experiment [2]. The duobinary (DB) and alternate-mark-inversion (AMI) modulation formats [3-5] can out-perform OOK through the suppression of both linear and nonlinear transmission impairments. For example, NRZ-DB can be utilized for greater tolerance to dispersion [6], and both RZ-AMI and RZ-DB have shown increased nonlinear transmission performance at 42.7 Gb/s compared with OOK [3]. AMI and DB convey information via binary intensity levels, as in OOK, and the transmission benefits result from auxiliary phase modulation. As a result, AMI and DB can be received using simple square-law detectors and the additional complexity of coherent receivers is avoided.

It seems likely that future optical networks will incorporate disparate modulation formats depending on the reach and bitrate requirements of its various constituents. Some means of conversion between modulation formats will become an important network function. At high bitrates this conversion process may benefit from an all-optical implementation where savings in energy consumption over optical-electronic-optical approaches may be possible [7]. The all-optical generation of DB and AMI could also be advantageously employed in high-bandwidth transmitters. Kang, *et al* [8], have pointed out that optical signal generation beyond 40 Gbaud is hampered by the stringent requirements on various electronic signal processing components and RF drive amplifiers. They propose the use of optical time-division multiplexing and all-optical modulation converters to push beyond these limits.

In this work we report on an experimental demonstration of an active all-optical system which translates RZ-OOK to RZ-AMI or RZ-DB at 42.6 Gb/s [9]. The fast optical nonlinearity is provided by semiconductor optical amplifiers (SOAs) which are capable of providing large phase shifts with relatively small input powers and are particularly attractive in terms of photonic integration potential. In these experiments, four SOAs are hybrid-integrated with planar silica waveguides making a pair of optical gates. This dual-gate scheme offers the potential for further integration, scaling to higher bitrates, and is flexible in its ability to easily change between AMI and DB output formats. Though passive approaches are possible for the all-optical generation of AMI from an OOK input [10], we anticipate that our SOA-based active approach has the potential for 3R regeneration [11] and the choice of output wavelength is arbitrary.

In Section 2 we show that an all-optical XOR gate can be used as the modulation converter and discuss its theory of operation. Numerical results for 40 Gb/s DB generation are shown in Section 3. Section 4 contains the experimental results for 42.6 Gb/s and 10.65 Gb/s all-optical modulation conversion of OOK to both AMI and DB. In Section 5 we discuss the use of an additional optical input signal to suppress patterning in an all-optical XOR gate and model its impact on DB generation at bitrates beyond 40 Gb/s. We provide concluding remarks in Section 6, and derivations of the expected spectral shapes of DB and AMI signals are shown in the Appendix.

2. Theory of operation

The duobinary (DB) and alternate-mark-inversion (AMI) linecodes can be generated using delay-and-add and delay-and-subtract operations, respectively [1, 12]. Data is conveyed via pulse amplitudes, as in on-off-keying (OOK), and the mathematical operations impress the characteristic auxiliary phase modulation on the pulses. In order to restore the original input message to the AMI or DB output (in intensity), a simple precoding or decoding is necessary. The additional $(0,\pi)$ phase modulation for DB and AMI is qualitatively different: DB marks only flip phase when separated by an odd number of spaces and AMI marks always flip phase regardless of their spacing.

The delay-and-add and delay-and-subtract operations are summarized below in Eqs. (1)-(2) for a binary input signal $x[n]=\{0,1\}$ and output signals $y_{AMI}[n]$ and $y_{DB}[n]$:

$$y_{AMI}[n] = x[n] - x[n-1] \tag{1}$$

$$y_{DB}[n] = x[n] + x[n-1] - 1, \tag{2}$$

where y_{AMI} and y_{DB} are the AMI and DB sequences, respectively. Both output sequences use the symbols $\{-1, 0, +1\}$. The -1 has been included in Eq. (2) to force the mean signal value to zero, consistent with optical DB signals used in practice. We also note from Eq. (2) that DB can be calculated using a subtraction operation as follows:

$$y_{DB}[n] = x[n] - (1 - x[n-1]) = x[n] - \bar{x}[n-1], \tag{3}$$

where the -1 has been utilized to invert the delayed input signal. We will later show that Eq. (3) is crucial for producing a high-quality signal with the all-optical gates.

Equations (1)-(3) indicate that an all-optical gate capable of calculating sums and differences can be utilized to generate DB and AMI outputs. Such a gate can be realized using an SOA-based Mach-Zehnder interferometer (MZI) and is shown below in Fig. 1 with four inputs (data inputs A and B, a probe input, and a pattern suppression signal input) and a pair of output ports (Δ and Σ). We will ignore the pattern suppression signal input until later in Section 5. The injected probe (λ_{probe}) propagates through the two SOAs which can change both the amplitude and phase of the probe. With no data input to the MZI, the two path lengths are identical, and the probe constructively interferes at the Σ port and destructively interferes at the Δ port.

The gate is shown in the well-known push-pull configuration [13, 14]. This allows short switching windows, but will not eliminate patterning. A pulse injected only into input port A, denoted as input state (1,0), is split between SOA1 and SOA2. The "push" pulse first saturates SOA1, and due to both cross-gain (XGM) and cross-phase modulation (XPM), the interference conditions for the probe are changed, opening a switching window for λ_{probe} at the output ports. The other pulse copy is delayed by τ_{pull} and this "pull" pulse enters SOA2 and closes the switching window.

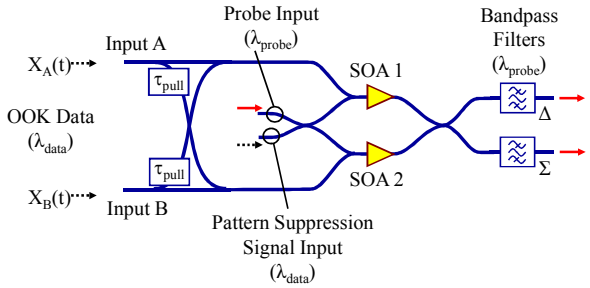


Fig. 1. All-optical logic gate with XOR-type architecture.

The logical operation of this gate can be predicted using a transfer function analysis to derive the relative amplitude and phase relationships between the various MZI output states. It is straightforward to show that the transfer functions describing the outputs from the Δ and Σ ports of the interferometer are given below:

$$H_{\Delta} = \frac{1}{2}\left(e^{-\frac{\varphi_1}{\alpha}} e^{j\varphi_1} - e^{-\frac{\varphi_2}{\alpha}} e^{j\varphi_2} \right) \tag{4}$$

$$H_{\Sigma} = \frac{1}{2}\left(e^{-\frac{\varphi_1}{\alpha}} e^{j\varphi_1} + e^{-\frac{\varphi_2}{\alpha}} e^{j\varphi_2} \right) \tag{5}$$

where the XPM shifts for SOA1 and SOA2 are given by φ_1 and φ_2, respectively. The XGM on the probe is captured via the α-factor within exponential terms; these exponentials decrease with increasingly large XPM shifts, i.e. both α and φ are positive-valued. In the derivation of Eqs. (4) and (5), the unsaturated gains through the SOAs have been normalized to unity.

The logical output states from the XOR gate, as electric field quantities, can be calculated using Eqs. (4) and (5) and some representative values are summarized below in Table 1. The binary values in the "A" and "B" columns indicate whether or not a pulse is injected into Input A and Input B, respectively. The second row in Table 1, for example, is calculated assuming that a pulse enters Input A only, and corresponds to $\varphi_1 > 0$ and $\varphi_2 = 0$. The pull inputs in Fig. 1 are neglected for the sake of clarity in this analysis.

Table 1. All-Optical Gate Output Logic

		$\alpha = \infty$	$\varphi = \pi$	$\alpha = 5$	$\varphi = \pi/2$
A	**B**	$\mathbf{H_\Sigma}$	$\mathbf{H_\Delta}$	$\mathbf{H_\Sigma}$	$\mathbf{H_\Delta}$
0	0	+1	0	+1	0
1	0	0	-1	$0.62e^{j0.2\pi}$	$0.62e^{j0.8\pi}$
0	1	0	+1	$0.62e^{j0.2\pi}$	$0.62e^{-j0.2\pi}$
1	1	-1	0	$0.73e^{j0.5\pi}$	0

Two sets of calculations are shown in Table 1. The first group (columns 3 and 4) corresponds to an infinite α-factor and a possible XPM shift of π (indicated by φ in the table), and the second group (columns 5 and 6) shows the results for a representative α-factor of 5 and potential XPM shift of $0.5 \cdot \pi$. The first group of calculations suggests that the XOR output ports operate in the following way:

$$H_\Delta \propto B - A \tag{6}$$

$$H_\Sigma \propto 1 - (A + B) \tag{7}$$

Eqs. (6) and (7) correspond to Eqs. (1) and (2) suggesting that AMI and DB can be obtained at the Δ and Σ ports, respectively. However, the calculations shown in the first group (columns 3 and 4) assume that the SOAs exhibit zero XGM (the infinite α-factor) and have exact π radian XPM shifts. The infinite α-factor assumption is unrealistic in practice, and π phase shifts generally become increasingly difficult at high bit-rates.

The second group of data (columns 5 and 6) represent more realistic calculations, where XGM is included and the XPM shift is somewhat smaller. In this data set, Eq. (7) is clearly no longer correct for the Σ port. The spaces are very poorly extinguished and the two mark vectors are unequal in amplitude and are not separated by π radians. However, Eq. (6) still holds true for the Δ output port, as good zeros are obtained and the two mark vectors are equal in amplitude and separated by π radians. The only consequence of the XGM and smaller XPM shift is that the output mark amplitude is reduced.

The key conclusions here are that the Δ output port is much more appealing for logical operations, and when using this port the only criterion for perfect phase inversions on the output pulses is symmetrical XPM shifts in the two SOAs. We also expect better exploitation of the MZI's regenerative abilities [11, 15] using the Δ port. We conclude that the difference calculation at the Δ port must be used for both AMI and DB generation as consistent with Eqs. (1) and (3) given above. We have already shown via numerical modeling that the Δ port can generate a high-quality AMI output signal [14].

3. Numerical modeling of 40 Gb/s duobinary generation

We now report on modeling results for the operation of the all-optical XOR gate as an OOK to DB modulation converter. We have previously reported similar modeling results for AMI modulation conversion in [14]. The computer model is based on a travelling-wave rate-equation analysis and the coupled partial differential equations are solved using a fourth-order Runge-Kutta algorithm. The XGM and XPM on the probe are captured via gain and refractive index changes calculated using a density matrix approach, eliminating the need for an α-factor approximation such as that used above. Ultrafast gain saturation and recovery are captured through carrier heating calculations. Further details on the numerical model can be found in [16], and we use similar device parameters here.

The 2mm SOAs are each injected with 350 mA of current producing a mean saturated gain of 19 dB peaking at ~ 1552 nm. The saturated gain and phase recovery times (10% to 90%) are ~ 15 ps and 24 ps, respectively, and so we expect pattern effects to be

minimized in these simulations. This will allow the operation of the gate to be more clearly seen, and the impact of carrier density recovery times on the results will be discussed in further detail in subsequent sections. The 1548.51 nm OOK input signal into port A is the logical inverse of a standard 2^7-1 pseudorandom binary sequence (PRBS) and the input to port B is the non-inverted PRBS sequence delayed by one bit period. The 2 ps push and pull-pulses have peak powers of 1 mW and 0.3 mW, respectively, at the SOA inputs. The pull-pulse delay, τ_{pull}, is set to 8 ps. A 100 μW continuous-wave (cw) signal injected into each SOA at 1550.92 nm is used as the probe. The output power is calculated at port Δ and shown in Fig. 2 (bottom trace) along with the input signals into ports A (top trace) and B (middle trace).

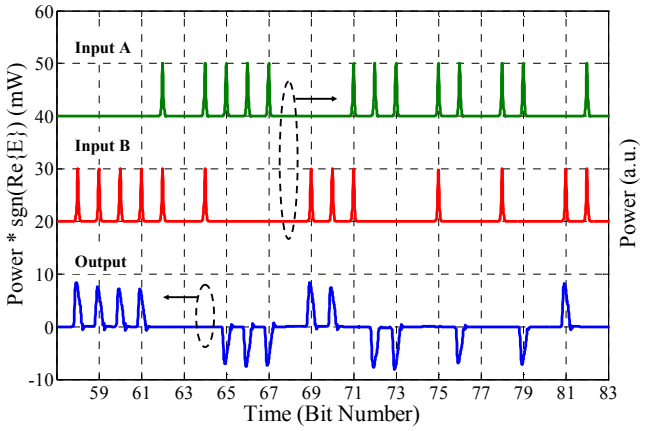


Fig. 2. The all-optical gate RZ-OOK inputs and RZ-DB output. $Re\{E\}$ is the real part of the output electric field, and E has been rotated in the complex plane so as to be aligned with the real axis.

The amplitude of the bottom trace in Fig. 2 clearly shows the XOR operation, i.e. modulo 2 addition, between inputs A and B. The sign of the DB output power shows the pulse-to-pulse phase changes as pulse inversions around the zero-power level. The phase inversions occur only when there is an odd number of zeros between pulses which is consistent with DB modulation.

The output modulation format also has particular features in its spectrum. In the Appendix we use Fourier Transforms to derive the following spectral shape for baseband DB signals:

$$\widetilde{Y}_{DB} = \widetilde{U}(2\pi\frac{F}{T})\cdot\left\{2\cdot\widetilde{x}(2\pi F)\cdot e^{-j\pi F}\cdot\cos(\pi F) - \sum_{n=0}^{M-1} e^{-j2\pi nF}\right\} \tag{8}$$

where $\widetilde{Y}_{DB}$, $\widetilde{U}$, and $\widetilde{x}$ are the Fourier Transforms of the DB signal and a single pulse, and the Discrete-Time Fourier Transform (DTFT) of $x[n]$, respectively. F is the dimensionless normalized frequency, i.e. $F = f \bullet T$, where f is the frequency (Hz) and T is bit period (s), respectively. In accordance with the discussion in the Appendix, Eq. (8) indicates that the amplitude of the OOK spectrum ($\widetilde{x}$) will be modified by a cosine function producing nulls at half-fractional values of the normalized frequency, i.e. $F = \pm 0.5, \pm 1.5, \ldots$ The negative exponential functions suppress the DC component (or the carrier for an optical signal) and modulation-harmonics at $F = 0, \pm 1, \pm 2, \ldots$

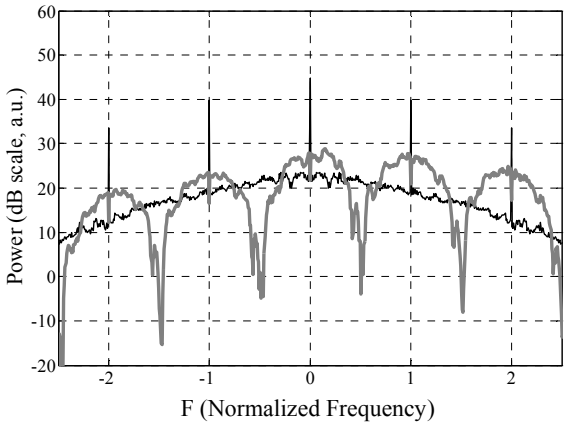


Fig. 3. Output DB (grey) and OOK (black) spectra calculated from the electric field output from the XOR gate. Spectral features consistent with Eq. (8) can be clearly seen. The frequency axis is centered at the carrier and normalized to the bitrate.

The spectrum calculated from the modeled output electric field from the XOR gate is shown in Fig. 3. Also shown for comparison is the OOK spectrum that results if the phase modulation is stripped from the output field. The DB spectrum agrees with the features predicted in Eq. (8). The phase inversions on the output pulses lead to DC component and modulation harmonic suppression and well-defined nulls between the DC component and modulation harmonics. A similar DTFT analysis for AMI is also shown in the Appendix, and these predicted spectral features will be compared with the DB and AMI experimental results discussed in the next section. The results in [14] include similar time-domain and spectral modeling data for the XOR gate operating as an AMI generator.

4. 42.6 Gb/s experimental results

We now present the experimental results for 42.6 Gb/s all-optical modulation conversion of input OOK to output DB and AMI. As discussed in the previous sections, non-delayed and delayed replicas of the input OOK data are required for input to the XOR gate. One of these copies is then either non-inverted or inverted to produce AMI or DB, respectively. We utilize a Dual-Output Wavelength Converter (DOWC) optical gate [17] to produce two copies of the input data, which in turn drive the XOR gate as modeled above. This SOA-MZI-based optical gate has two output ports which can be easily reconfigured to produce either inverted or non-inverted copies of the input data. This scheme is shown below in Fig. 4, and a detailed depiction of the DOWC is shown below in Fig. 5.

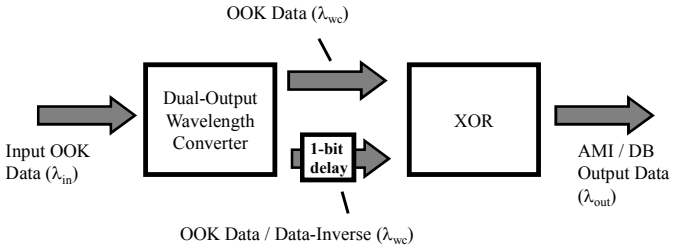


Fig. 4. Conceptual diagram of the all-optical modulation converter incorporating two optical gates.

The DOWC is not strictly necessary for producing AMI, but the extra wavelength conversion allows an arbitrary choice for the final output signal wavelength, including the original input wavelength. We also note that the output pulse sequence will generally differ from the input sequence, and a conventional transceiver precoding or decoding can be used to recover the message. This step is omitted here in this proof-of-concept experiment.

A detailed picture of the experimental setup is shown in Fig. 5. The pair of all-optical gates was produced by CIP Technologies. The proprietary buried-heterostructure SOAs are fabricated using III-V materials and then hybrid-integrated with low-loss planar silica waveguides. The saturated gain recovery times are measured on the SOAs to be ~ 28 ps. The DOWC has two MZI outputs each with full interferometer bias control. These are necessary for independent optimization of the non-inverted and inverted outputs, particularly when the dynamic XPM shifts are less than π radians. The XOR gate also has integrated push-pull power splitters and delays providing convenient optimization of the relative optical pumping of the two SOAs. Further details on the operation of SOA-based MZIs can be found in references [16, 18].

The RZ-OOK data used at the input to the setup is created by modulating the output of a 10.65 GHz mode-locked laser with a standard 2^7-1 pseudo-random bit sequence (PRBS) and passively multiplexing to 42.6 Gb/s. The short pattern length is necessary due to the design of the passive data multiplexer. On the left-hand side of Fig. 5, the input data at wavelength λ_{in} = 1562.3 nm enters a 3-dB power splitter which provides the push and pull inputs to the DOWC. Variable time delays and attenuators ensure proper timing and relative amplitudes of the two input signals. Fiber-based polarization controllers allow control of the optical field orientation injected into the SOAs. The output from a 42.6 GHz mode-locked laser provides the clock input at wavelength λ_{WC} = 1556.1 nm to the DOWC. The phase shifter (i.e. interferometer bias) on the upper MZI output is adjusted to produce a wavelength-converted copy of the Data input to the DOWC. The phase shifter on the lower output is independently adjusted to either produce Data or Data-Inverse, corresponding to AMI or DB at the XOR output, respectively. The clocked input to the DOWC is necessary here so that Data-Inverse is generated as an RZ signal.

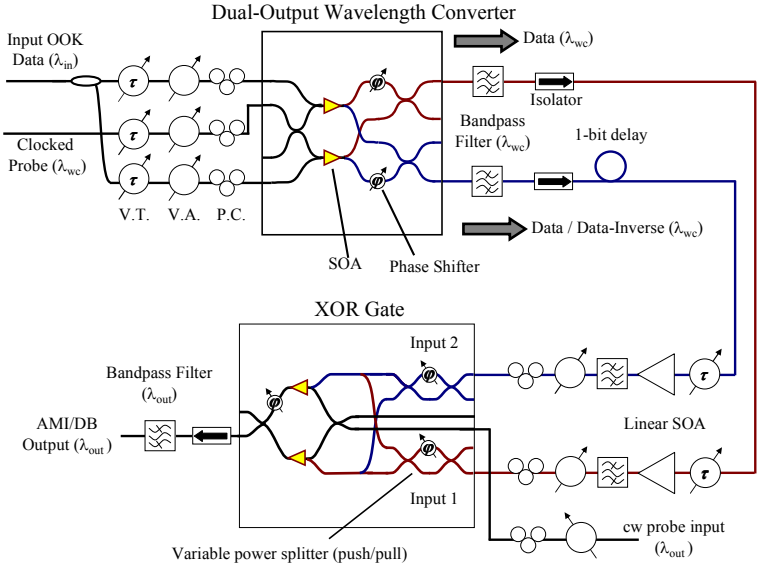


Fig. 5. Detailed experimental setup. V.T., V.A., and P.C. are variable time delay, variable attenuator, and polarization controller, respectively.

The outputs from the DOWC are then transmitted to the integrated XOR gate where variable time delays allow adjustment of the necessary 1-bit delay between the two signals. The continuous-wave (cw) probe signal injected into the XOR gate is at wavelength λ_{out} = 1562.5 nm. Numerical values for the measured power levels are given in Table 2. P_{push}, P_{pull}, P_{clock}, P_1, P_2, and P_{cw} listed in Table 2 are the push, pull, and clock input powers to the DOWC and Input 1, Input 2, and cw input powers to the XOR gate, respectively. P_{out} is the signal output power at λ_{out} from the XOR gate. The SOAs sink ~ 450 mA and ~ 470 mA for the DOWC and XOR gate, respectively.

Table 2. Experimental Parameters

	Power (dBm)					
Output Modulation	P_{push}+ P_{pull}	P_{clock}	P_1	P_2	P_{cw}	P_{out}
AMI	-7.0	-2.5	0.1	2.2	-1.1	-6.9
DB	-1.0	-0.3	4.5	6.7	2.5	-5.6

Evidence for the correct output modulation can be seen on the XOR output spectra [9], which are shown in Figs. 6a and 6b. Fig. 6a compares the output DB spectrum (black line) with the OOK output spectrum (gray line) produced by turning off Input 2 to the XOR gate. The spectra are measured using a 0.015 nm resolution and then plotted versus the normalized frequency ($F = f \bullet T$) centered at the cw carrier. The two spectra are also normalized so that their integrated powers are equal. The OOK spectrum in Fig. 6a displays the expected carrier and modulation-harmonic peaks at integer values of the normalized frequency, i.e. at multiples of the bitrate. The other bump-like features in the measured spectra between the modulation peaks are artifacts of the short PRBS pattern.

The DB spectrum in Fig. 6a exhibits characteristic nulls at fractional values of the normalized frequency ($F = \pm 0.5, \pm 1.5$, etc) as well as suppression of the carrier and modulation-harmonics ($F = 0, \pm 1, \pm 2$, etc). Clear and open output eyes corresponding to each spectrum are also shown, which have extinction ratios of 13.6 dB (OOK) and 11.8 dB (DB) as measured from the equivalent-time scope traces. Similarly, Fig. 6b shows the AMI output spectrum (black line) plotted along with the OOK output spectrum (gray line) when Input 1 to the XOR gate is turned off. In this case, the AMI spectrum shows the expected nulls at integer values of the normalized frequency ($F = 0, \pm 1, \pm 2$, etc). The output eyes are shown in the upper corners and have measured extinction ratios of 12.2 dB (OOK) and 13.2 dB (AMI).

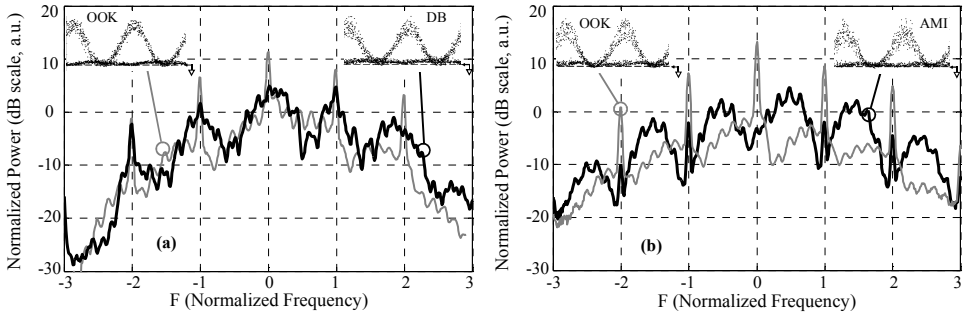


Fig. 6 (a) The DB (black) and OOK (gray) output spectra. (b) The AMI (black) and OOK (gray) output spectra. In both plots the independent axis shows the normalized frequency, F, which has been centered at the carrier and scaled by the bit period ($F = f \bullet T$).

The measured spectra in Figs. 6a and 6b show some deviation from the *sin(πF)* and *cos(πF)* spectral shapes predicted by Eqs. (A4) and (A6) in the Appendix, in particular the partial re-emergence of the modulation-harmonics. We believe that this spectral characteristic manifests, in part, due to the presence of patterning on the output signal, which is expected since the bit period is comparable to the gain recovery time of the SOAs. We have shown in previous numerical experiments the relationship between amplitude and phase patterning on the AMI output from the XOR gate [14]. In this earlier work we noted that the temporally correlated nature of the two XOR input signals leads to unequal average phase shifts for the 0 and π phase-shifted output pulses. This breaks the operational symmetry discussed in Section 2 as being necessary for perfectly inverted output pulses and should result in some reduction in carrier suppression. This phenomenon was denoted as phase compression to describe the subsequent sub-π mean phase shift between the two sets of output marks. Intensity patterning is evident on the eye diagrams in Fig. 6 and this suggests the presence of phase patterning and phase compression as well. Other operational and device asymmetries may result in further distortion of the output spectra, yet despite these factors, the suppression of the carriers in the DB and AMI output spectra are measured to be at least ~ 6.4 dB and ~ 16.5 dB, respectively, with respect to the OOK carrier.

The pattern effects and phase compression should be reduced if the input signal data rate is decreased. This allows the SOAs to reach a more recovered state before being pumped by the next data pulse. We repeated the experiment described above at a lower data rate of 10.65 Gb/s using a similar experimental setup. The probe into the XOR gate in this case is taken from the same clock source providing pulses for the data modulator feeding the DOWC (i.e. Input OOK Data in Fig. 5). The output spectra were measured and are shown below in Fig. 7.

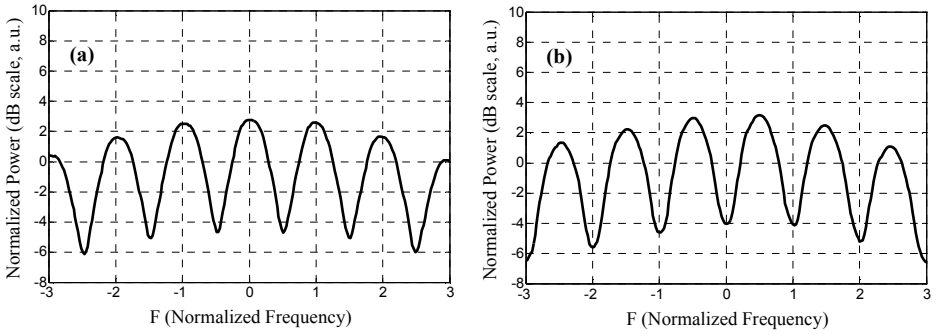


Fig. 7. (a) DB and (b) AMI spectra measured for 10.65 Gb/s modulation conversion. In both plots the independent axis shows the normalized frequency, F, which has been centered at the carrier and scaled by the bit period ($F = f \bullet T$).

The spectra show excellent carrier and modulation-harmonic suppression and also clearly display the *cos(πF)* and *sin(πF)* spectral envelope shape predicted by the Fourier analysis described in the Appendix and given in Eqs. (A4) and (A6).

These results suggest that by employing faster SOA configurations, the output signals at 42.6 Gb/s can be improved. This could be accomplished using nanophotonic devices such as quantum dots [19] or perhaps by utilizing alternate filtering schemes [20-22]. We have also recently demonstrated experimentally the use of a pattern suppression scheme using an SOA-based MZI wavelength converter [17]. This technique utilizes the injection of an additional data-inverse signal into the probe input port of the gate, effectively equalizing the optical energy in the SOAs in every bit period. We believe such a technique can be adapted to operate with XOR gates and we discuss related numerical results in the next section.

5. Pattern suppression signal scheme

The 10.65 Gb/s spectra shown in Fig. 7 suggest the importance of the carrier density recovery time, and the impact of patterning, with regard to signal output quality. Bischoff, *et al*, [23] and Webb, *et al*, [17] have demonstrated that pattern effect mitigation can be achieved in SOA-based MZI optical gates using a data-inverse input signal. In this prior work a logically-inverted signal was injected into one of the interferometer input ports (i.e. not a data input). A signal injected into this port will simultaneously excite the two SOAs, and the resultant XGM and XPM on the probe does not open the MZI switch. In this way, a pulse can be injected during a data space (no data pulse) in order to balance the optical energy in each bit period. This prevents the SOA gain from recovering to a high value, and patterning can be reduced through the suppression of large output marks after a string of spaces. We will call this additional input signal the Pattern Suppression Signal (PSS).

There are two data input signals to the XOR gate (see Fig. 1) and so two data-inverse signals are necessary to appropriately balance the input energy in each bit period. The PSS is constructed by incoherently summing the powers of the RZ logical-inverses of the two data inputs producing a three-level signal. The PSS is injected into the unused interferometer input port, as shown in Fig. 1, and the PSS is timed so that the pulses arrive at the SOAs between the push and pull pulses, i.e. $\tau_{PSS} = 0.5 \bullet \tau_{pull}$ and $\tau_{pull} \sim T/3$, as depicted in Fig. 8.

Fig. 8 shows that for input state (1,1) there is no PSS pulse input to the XOR gate, where (1,1) denotes an input data pulse into both SOA1 and SOA2, respectively. For input states (1,0) and (0,1) a PSS pulse is injected between the push and pull pulses at time τ_{PSS}. Finally, for input state (0,0) there is a PSS pulse injected with twice the power. Note that the PSS needed for both AMI and DB is constructed from the data and data-inverse signals readily available in the experimental setup shown in Fig. 5. This suggests that the appropriate signal splits and delays for generating the PSS can be integrated with the optical gates.

Using the same model described in Section 3, we model the effect of the PSS on the XOR gate output signal for DB modulation conversion, and we expect qualitatively similar results for AMI. The PSS is comprised of pulses of the same width and wavelength as the data inputs. The ideal PSS pulse amplitudes are identified by increasing the PSS signal power in the model until the patterning on the output DB signal is minimized.

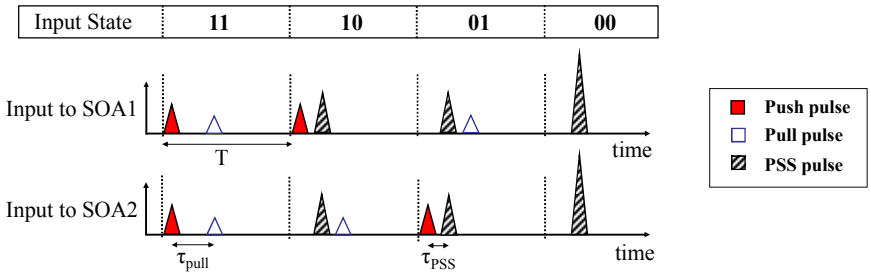


Fig. 8. Input signal pulse timing to XOR gate for the pattern suppression scheme.

At 80 Gb/s the signal bit period is slightly smaller than the SOA gain recovery time (~ 15 ps) a scenario comparable to the 42.6 Gb/s experiment described above in Section 4. The modeled optical pulses are 2 ps in width, and the push and pull powers into the SOAs are 1 and 0.6 mW, respectively. The push-pulse to pull-pulse delay (τ_{pull}) is 4.2 ps. The model predicts ideal pulse peak powers for the three-level PSS at 80 Gb/s to be 0, 1.27, and 2.54 mW. These PSS pulse powers are higher than would be expected in order to balance the total input pulse energy in each bit period for all possible data inputs. The model suggests that the higher PSS power is needed to compensate for ultrafast gain compression, i.e. carrier heating in this model.

The 80 Gb/s output constellations without and with the PSS are shown in Figs. 9a and 9b, respectively. Patterning in both the symbol amplitude and phase is evident in Fig. 9a, and the phase patterning is evidently significantly larger than the amplitude patterning. This is consistent with the observations in [24] where Kang, *et al*, attribute the larger phase patterning to the longer recovery time of the SOA phase compared to the gain. The phase patterning manifests as both angular spreading and a sub-π radian mean angular offset between the two sets of output marks. This non-ideal sub-π phase modulation arises due to the temporally correlated nature of the two XOR gate inputs. The result of the correlated inputs is that the 0-modulated and π-modulated output pulses are each created at times in which the SOAs, on average, are at different levels of saturation. The XPM shifts experienced by the probe now differ for the two groups of output marks, and in this way, the pattern effect breaks the operational symmetry needed for ideal phase modulation on the output pulses. See Eq. (4) in Section 2 for the XOR gate's transfer function, as well as [14] for further discussion. This non-ideal symbol separation is captured by the phase compression, δ, where

$$\delta \equiv 1 - \frac{\Delta\theta}{\pi} \tag{9}$$

and Δθ is the mean angular separation between the two sets of output marks as shown in Fig. 9a. δ goes to zero as the mark phase modulation approaches an ideal π radians. The uncompensated output signal in these results exhibits a phase compression of $\delta \sim 0.16$.

Upon application of the PSS, both the amplitude and phase patterning in the output constellation shown in Fig. 9b clearly decrease and δ drops to $\sim 9.6 \cdot 10^{-3}$. The patterning in mark power at the output, defined as the ratio of maximum mark peak-power to minimum mark peak-power [25], decreases from 2.2 dB to 0.49 dB. However, a trade-off arises with decreasing signal output power accompanying increased patterning suppression due to the increased state of saturation of the SOAs with the PSS input. The model predicts a drop in mean output power of 5.8 dB with the PSS on.

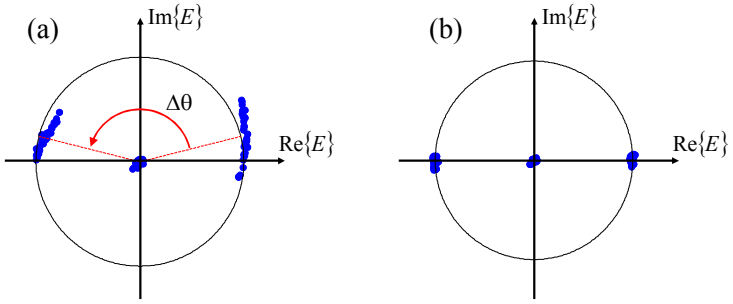


Fig. 9. DB output constellations (a) without and (b) with PSS.

The DB output eyes are also calculated and plotted in Fig. 10a and Fig. 10b with the PSS turned off and turned on, respectively. Patterning is clearly evident on the mark heights of the unoptimized output eye in Fig. 10a. The eye is improved upon application of the PSS, as shown in Fig. 10b, and the eye opening [16] shows a 0.86 dB improvement. The vertical-axis scaling on Figs. 10a and 10b also indicates the penalty in output power realized for suppressing the patterning with the PSS. Fig 10b also indicates some narrowing of the output pulse, and we expect that the pulse shape can be a function of several variables including SOA saturation (carrier density recovery speedup through the holding beam effect [26]) and the pull delay (τ_{pull}). The pull delay can be engineered to restore the output pulse width to the desired value.

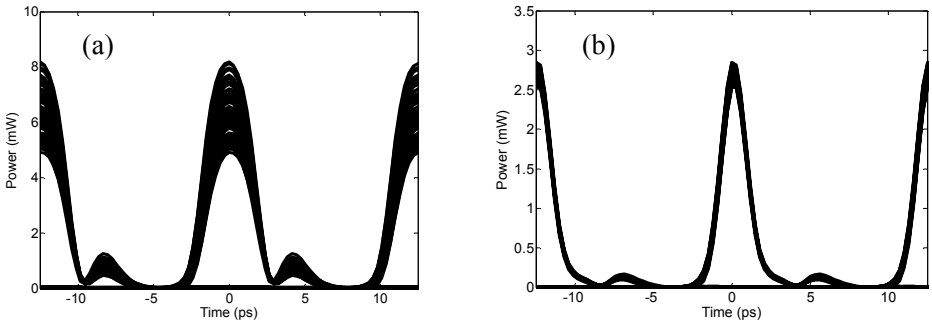


Fig. 10. Eye diagrams for DB output (a) PSS off and (b) PSS on.

These results suggest that the application of the PSS allows the operational bandwidth of the modulation converter to be extended to bitrates well beyond the carrier density recovery rate. We test this idea by repeating the numerical experiment at 40, 120 and 160 Gb/s. The analysis in [27] by Xu, *et al*, suggests that a 2^7-1 PRBS is sufficient to estimate the patterning effects at 160 Gb/s given the fast 15 ps gain recovery times modeled here. We consider the performance of the modulation converter in terms of the output mark patterning and the drop in output power resulting from utilization of the PSS. The signal timing and pull powers are adjusted appropriately for each bitrate, and all other modeling parameters are kept constant. The results are summarized below in Fig. 11.

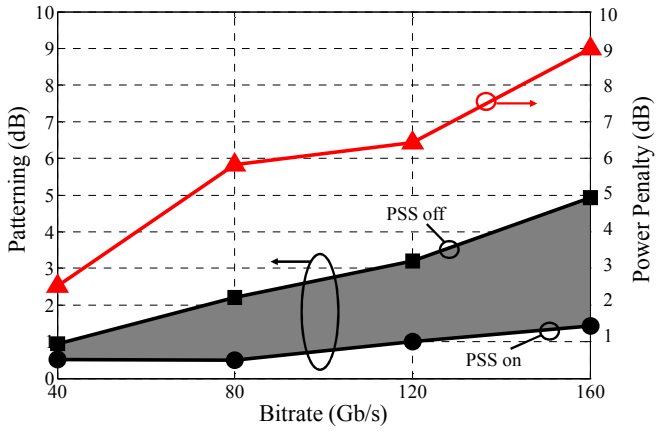


Fig. 11. Output mark patterning and output power penalty vs. bitrate

The line in Fig. 11 with square markers shows the output mark patterning without use of the PSS. Here the patterning is defined as the ratio of largest mark peak-power to lowest mark peak-power and is expressed in dB. As expected, the patterning becomes worse as the bitrate increases and the SOA gain is less able to recover between data pulses. With no PSS the output signal accumulates an extra 4.0 dB in patterning at 160 Gb/s. However, the line with circle markers shows the variation in patterning with bitrate when the PSS is turned on. The patterning accumulates much more slowly providing a 0.42 dB improvement at 40 Gb/s (where patterning is not too severe to start) and an even larger 3.5 dB improvement at 160 Gb/s.

However, this improvement to the output signal cannot be extended indefinitely, as the power penalty curve shows (triangles). This line shows the reduction in mean output power due to application of the PSS and increases from a 2.5 dB penalty at 40 Gb/s to a 9.0 dB penalty at 160 Gb/s. In terms of evaluating where this device would function in an optical

network, this power penalty could negatively impact device cascadability, receiver performance, etc.

In this PSS scheme it is possible that temporally adjacent and coherent pulses will partially overlap in time and interfere with each other. In a physical implementation of this PSS scheme this could lead to unintended power levels in the SOAs (through destructive and constructive interference), and possibly low frequency oscillations in the output powers as thermal effects modulate the relative phases of the overlapping pulses. This undesirable interference can be suppressed using polarization or wavelength diversity in the input signals. Such diversity would also provide a convenient method for incoherently summing the data pulse powers to construct the PSS.

6. Conclusions

We have experimentally demonstrated a 42.6 Gb/s OOK-to-AMI and OOK-to-DB all-optical modulation converter consisting of two hybrid-integrated SOA-based MZI gates: a Dual-Output MZI and an XOR gate. We show that the DB and AMI formats are theoretically predicted at the output of the XOR gate using a transfer function analysis as well as a comprehensive computer-based SOA model. The experimental results indicate open output eyes and spectral features matching those predicted using a simple Fourier Transform analysis of the XOR gate operation. Comparison with 10.65 Gb/s data suggests the importance of the carrier density recovery time and the impact of the pattern effect on the quality of the output signals. We address this issue by outlining a new scheme for suppressing the patterning effect in XOR gates, which is similar to techniques already successfully demonstrated in simpler SOA-based structures. Using this pattern suppression technique, we believe that this modulation converter can be utilized at bit rates well beyond the carrier density recovery rate. This dual-gate active approach to modulation conversion has the potential for 3R regeneration, can output to an arbitrary wavelength (within the SOA gain bandwidth), and can easily change between DB and AMI outputs. The system is also amenable to further photonic integration and subsequent reductions in power consumption. We believe this all-optical approach to DB and AMI generation could impact implementations of both high-speed transmitters and modulation converters.

Acknowledgments

This work was supported by the Science Foundation Ireland under grant 06/IN/1969.

Appendix

Here we will derive the expected spectral shapes of alternate-mark-inversion (AMI) and duobinary (DB) baseband output signals. Key features from these spectra can be compared with the measured optical spectra to indicate the output modulation format. The output signal, $Y(t)$, from the XOR gate can be represented as a comb of identical pulses each with temporal shape $U(t)$. This comb is modulated by a three-level discrete message $y[n]$ of length M:

$$Y(t) \approx \sum_{n=0}^{M-1} y[n] \cdot U(t - nT), \tag{A1}$$

where T is the bit period and $y[n]$ is zero for $n < 0$ and $n > M$-1. The Fourier Transform of $Y(t)$ can be written as

$$\begin{aligned}\widetilde{Y}(2\pi f) &= \int_{-\infty}^{\infty} Y(t)e^{-j2\pi ft}\,dt \\ &= \sum_n y[n]\int_{-\infty}^{\infty} U(t-nT)e^{-j2\pi ft}\,dt \\ &= \widetilde{U}(2\pi f)\sum_n y[n]e^{-j2\pi fnT} \\ &= \widetilde{U}(2\pi f)\cdot\widetilde{y}(2\pi fT)\end{aligned} \tag{A2}$$

where j is the imaginary number $\sqrt{-1}$ and f is the frequency. The time-shift property of the Fourier Transform has been utilized on $U(t)$ to generate the pulse spectrum, $\widetilde{U}(2\pi f)$, and $\widetilde{y}(2\pi fT)$ is the Discrete-Time Fourier Transform (DTFT) of the message $y[n]$. Equation (A2) indicates how the pulse spectrum is modified by the modulation spectrum.

The spectral envelope of the pulse is the same for AMI and DB, and it is the transform of the message, $y[n]$, that changes. We first consider Eq. (1) from the main text above, which describes AMI:

$$y_{AMI}[n] = \begin{cases} x[n]-x[n-1], & 0 \le n \le M-1 \\ 0, & otherwise \end{cases} \tag{A3}$$

where $x[n]$ is the binary (OOK) message being converted to AMI. We denote the DTFT of $x[n]$ as $\widetilde{x}(2\pi fT)$ and using the time-shift property of the DTFT, we can write the transform of Eq. (A3) as

$$\begin{aligned}\widetilde{y}_{AMI}(2\pi fT) &= \widetilde{x}(2\pi fT)\cdot\left(1-e^{-j2\pi fT}\right) \\ &= 2j\cdot\widetilde{x}(2\pi fT)\cdot e^{-j\pi fT}\cdot\sin(\pi fT)\end{aligned} \tag{A4}$$

This result indicates that on top of the OOK spectral shape due to the input signal modulation, $\widetilde{x}(2\pi fT)$, the AMI coding will impress in amplitude a $\sin(\pi fT)$ signature characteristic. This sine term suppresses the DC and modulation harmonic components on the AMI signal.

The DB linecoding is given by Eq. (2), assuming that the three-level discrete signal is centered at zero (note the AMI signal is also centered at zero)

$$y_{DB}[n] = \begin{cases} x[n]+x[n-1]-1, & 0 \le n \le M-1 \\ 0, & otherwise \end{cases} \tag{A5}$$

and the DTFT of Eq. (A5) produces

$$\widetilde{y}_{DB} = 2\cdot\left[\sum_{n=0}^{M-1} x[n]e^{-j2\pi fnT}\right]\cdot e^{-j\pi fT}\cdot\cos(\pi fT) - \sum_{n=0}^{M-1} e^{-j2\pi fnT} \tag{A6}$$

where the transform for $x[n]$ has been written explicitly. The first term on the right hand side of Eq. (A6) contains a $\cos(\pi fT)$ which modifies the amplitude of the spectrum in a similar way to the sine term for AMI in Eq. (A4). The second term on the right-hand side produces

DC and modulation harmonic suppression for the DB signal. The DC suppression can be seen by calculating $\tilde{y}(2\pi fT = 0)$:

$$\begin{aligned} \tilde{y}_{DB}(f = 0) &= 2 \cdot \sum_{n=0}^{M-1} x[n] - \sum_{n=0}^{M-1} 1 \\ &= 2\frac{M}{2} - M \\ &= 0 \end{aligned} \tag{A7}$$

where we have assumed that $x[n]$ is a random signal with an equal number of marks and spaces. A similar result applies at the modulation harmonics where $fT = 0, \pm 1, \pm 2, \ldots$ Note that the suppressed DC components in Eqs. (A4) and (A6) correspond with the carrier in an optically modulated signal.